Journal of Alloys and Compounds 781 (2019) 371–377

Contents lists available at ScienceDirect

Journal of Alloys and Compounds

journal homepage: http://www.elsevier.com/locate/jalcom

Predicted semiconducting beryllium sulfides in 3D and 2D configurations: Insights from first-principles calculations

HPSTAR 694-2019

Ning Gong [a], Chunxing Deng [a], Lailei Wu [a, c, *], Biao Wan [a, b], Zhibin Wang [c], Zhiping Li [c], Huiyang Gou [b, c, **], Faming Gao [c]

[a] State Key Laboratory of Metastable Materials Science and Technology, College of Material Science and Engineering, Yanshan University, Qinhuangdao, 066004, China
[b] Center for High Pressure Science and Technology Advanced Research, Beijing, 100094, China
[c] Key Laboratory of Applied Chemistry, College of Environmental and Chemical Engineering, Yanshan University, Qinhuangdao, 066004, China

ARTICLE INFO

Article history:
Received 8 October 2018
Received in revised form
17 November 2018
Accepted 28 November 2018
Available online 29 November 2018

Keywords:
First-principles calculations
Beryllium sulfides
Structural stability
Electronic property

ABSTRACT

Light-metal sulfides have attracted great attention due to the technological application as energy storage devices. Combining first-principles calculations with structure searching, sulfur-rich compounds were explored theoretically in Be-S system. Interestingly, our results identify a hitherto unknown stoichiometry BeS_2 in bulk and two-dimensional (2D) configuration. With the pressure increasing, BeS_2 in bulk adopts $P\bar{1}$ structure at ambient pressure, $C2$ phase over 1.6 GPa and then a cubic c-BeS_2 with unique S_2^{2-} dimmers up to 5.8 GPa. The monolayer penta-BeS_2 with Be_2S_3 pentagons and bilayer BeS structure are presented. Predicted c-BeS_2, 2D BeS_2 and BeS phases show a semiconducting character, interestingly, c-BeS_2 is found to have a direct band gap of 1.52eV. The discovery of unknown beryllium sulfides and the understanding of electronic and chemical bonding properties will provide prerequisite for the potential application in electrochemistry.

1. Introduction

The exploration of new materials for efficient energy storage and conversion represents one of the most attractive topics in the current energy-demanding world. Among diverse advanced energy materials, light-metal-sulfur batteries with extremely high theoretical energy density and low cost, such as Li-S [1–3], Na-S [4,5] and Mg-S [6–8] batteries, have been studied extensively for electrochemical energy storage. Li-S batteries have the high energy density of 2567 $Wh \cdot kg^{-1}$, and environmental benignity [9,10]. In addition, a Na-S room-temperature battery (RT Na-S) was produced with a high specific capacity of 1610 mA h g^{-1}, where sulfur cathode and Na anode enable a complete reduction to Na_2S [11]. Owing to the ability of providing two electrons for oxidation, magnesium has been found as a competitive anode material. In the case of Mg-S batteries, it is reported that the theoretical capacity of sulfur cathode and magnesium anode are 1675 and 2230 mA h g^{-1} respectively [12]. As a result, with the rapid progress and excellent properties of Li-, Na- and Mg-S batteries, it is natural to couple the sulfur cathode with other alkali mental or alkali earth metal anodes. Since beryllium is a relatively light element and could provide two electrons upon oxidization, the study of beryllium sulfides may also be helpful to apply Be-S system for energy storage devices within high chemical activity. Furthermore, the solid BeS proposed by Hwang et al. [13] could be used for the reversible storage of H_2.

Due to the small atomic radius and high ionization energy of Be atom, the studies of structural and electronic properties of beryllium compounds are of great interests [14,15]. In 1970, BeS with zinc-blende structure was prepared by the reaction of Be metal with H_2S [16]. In 1995, Luo et al. found that at about 69 GPa, BeS transform to NiAs-type structure [17]. Further, the transformation of BeS from zinc-blende to NiAs structure under 59 GPa was revealed by Narayana et al. [18] via X-ray-diffraction (XRD) analysis. Owing to the high toxicity of beryllium compounds [19], few experimental investigations have been reported up to now. The theoretical studies have uncovered some interesting properties by electronic analysis. For example, the potential applications for

* Corresponding author. State Key Laboratory of Metastable Materials Science and Technology, College of Material Science and Engineering, Yanshan University, Qinhuangdao, 066004, China.
** Corresponding author. Center for High Pressure Science and Technology Advanced Research, Beijing, 100094, China.
E-mail addresses: wll@ysu.edu.cn (L. Wu), huiyang.gou@gmail.com (H. Gou).

https://doi.org/10.1016/j.jallcom.2018.11.374
0925-8388/

optoelectronic and microelectronic devices of BeS have been suggested [20–22]. The wide band gap of bulk BeS (3.14eV in our results) made it possible for the production of blue-green laser diodes [23,24]. These discoveries stimulate further investigations on Be-S system to find more potential applications through theoretical methods.

In this work, we employed first-principle calculations and structural searching for the discovery of unknown beryllium sulfides under ambient and high pressures. The phase stabilities under pressure were checked by the calculations of formation enthalpy and phonon spectra. Strikingly, a new stoichiometric BeS_2 phase with pyrite structure (c-BeS_2) was revealed at 25 GPa, which has never been reported before. Besides, we also predicted a bilayer BeS phase (T-BeS) and a monolayer BeS_2 phase (penta-BeS_2). The structural feature and electronic analysis will be also discussed in detailed.

2. Computation details

To find out the possible candidates of Be-S system, the global structure searching of stable Be-S system was performed using the structure swarm global optimization methodology as implemented in the Crystal structure AnaLYsis by Particle Swarm Optimization (CALYPSO) package [25,26] interfaced with Vienna ab initio simulation package (VASP) [27], which can efficiently obtain the stable structures just depending on the given chemical compositions. We have performed structure searches at pressure of 0, 25, 50 and 100 GPa with up to six formula units (f.u.), the population size of each generation is fixed to 60, and the number of generation is set to 40. The generalized gradient approximation (GGA) of Perdew-Burke-Ernzerhof (PBE) [28] is used for the exchange-correlation potential within density functional (DFT) theory. We also calculated band structures based on Heyd-Scuseria-Ernzerhof (HSE06) hybrid functional [29,30]. The electron-ion interaction was described by pseudopotentials within the scalar relativistic projector-augmented wave (PAW) [31] approximation with $2s^2$ and $3s^23p^4$ as valence electrons for Be and S, respectively. During structure optimization, the energy precision to 1.0×10^{-5} eV, the maximum force was 1×10^{-2} eV/Å. A plane-wave cut-off energy of 500 eV and Monkhorst-Pack k-point meshes [32] with a grid spacing of $2\pi \times 0.03$ Å^{-1} were adopted for the first Brillouin Zone to ensure the energies converged to within 1 meV/atom. Phonon spectra were calculated using a direct supercell approach as implemented in PHONOPY code [33] with the forces calculated from VASP. The electronic structures and bonding properties were also carried out, including band structures, density of states (DOS), crystal orbital Hamilton populations (COHP) [34] and electron localization function (ELF) [35]-an electron localization indicator. The electron transfer was calculated via the Bader charge scheme [36]. Mulliken overlap populations (*MOP*) [37] were calculated using Cambridge Serial Total Energy Package (CASTEP) code [38]. Crystal figures were plotted by VESTA [39].

The chemical stabilities of various Be_xS_y compounds are checked by calculating the average atomic formation enthalpies up to 100 GPa. The stability with respect to elemental Be and S solids at each pressure is calculated with the equation below:

$$\Delta H_f = \left[H(\mathrm{Be}_x\mathrm{S}_y) - xH(\mathrm{Be}) - yH(\mathrm{S})\right]/(x+y)$$

ΔH_f is the relative enthalpy of formation per atom, $H(\mathrm{Be_xS_y})$ is the formation enthalpy per formula unit of the compound, H(Be) and H(S) are the calculated equilibrium energies of hexagonal-Be(S.G. $P6_3/mmc$), SI (S.G. *Fddd*) for 0 GPa, SII (S.G. $I4_1/acd$) for 25 and 50 GPa, and SIII (S.G. *Cmcm*) for 100 GPa [40], x and y are the number of Be and S atoms for stoichiometries, respectively.

3. Results and discussion

Our structural searches were carried out from Be_3S to BeS_4. The phase stability was examined firstly by the construction of the binary Be-S convex-hull (Fig. 1). $F\bar{4}3m$-BeS (denoted as c-BeS) is the only thermodynamically stable phase at 0 GPa. $Pa\bar{3}$-BeS_2 (denoted as c-BeS_2) shows on the convex hull starting at about 25 GPa, and it is energetically preferred at least up to 100 GPa. Besides, $P6_3/mmc$-BeS (donated as h-BeS) is lying on the convex-hull rather than c-BeS at 100 GPa. As seen in Table 1, the calculated deviation of the lattice parameters is about 0.3% from experimental results for c-BeS, indicating the reliability of the present calculations. To further clarify the phase transition pressure, the enthalpy differences of BeS (relative to $F\bar{4}3m$ phase) and BeS_2 (relative to $P\bar{1}$ phase) phases are calculated and plotted in Fig. 2 as a function of pressure. Both the zinc-blende type BeS (c-BeS) and its high pressure phase, NiAs type BeS (h-BeS) were reproduced by our structural searching. Notably, the transition pressure of 58.9 GPa is extremely close to the experimental result (59 GPa) [18] and previous prediction (58.46 GPa) [41], further validating the reliability of our predictions. The crystal structures for c- and h-BeS are plotted in Fig. 2a. It could

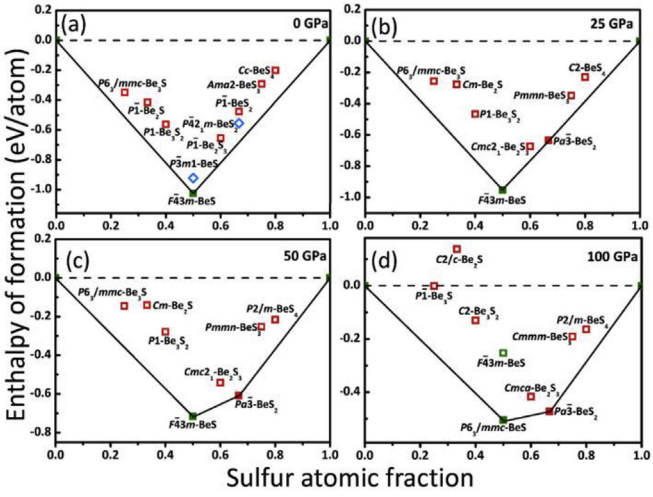

Fig. 1. The calculated formation enthalpies (ΔH) of various Be_xS_y compounds at pressure of (a) 0 GPa, (b) 25 GPa, (c) 50 GPa and (d) 100 GPa. The experimental phases are shown in green solid or open squares, our predicted bulk phases are shown in red solid or open squares, the layer phases are shown in blue open rhombuses. (For interpretation of the references to colour in this figure legend, the reader is referred to the Web version of this article.)

Table 1
Calculated lattice constants (a and c in Å), formation enthalpies (ΔH_f in eV/atom) at zero pressure and zero temperature, and band gaps (E_g in eV by GGA-PBE and HSE) for BeS and BeS_2 compared to available theoretical and experimental results.

phase	SG	a	c	ΔH_f	PBE-E_g	HSE-E_g	ref.
c-BeS	$F\bar{4}3m$	4.881		−1.025	3.14	4.03	
		4.878			3.10		Theo. [42]
		4.863			3.13		Theo. [43]
		4.745			2.75		Theo. [44]
		4.865			5.5		Exp. [18]
h-BeS	$P6_3/mmc$	3.311	5.264	−0.498	1.45	2.27	
		3.28	5.077				Theo. [41]
T-BeS	$P\bar{3}m1$	3.475		−0.922	3.79	4.79	
H-BeS	$P6_3/mmc$	3.460		−0.838	4.13	5.37	
		3.440			4.26		Theo. [45]
c-BeS_2	$Pa\bar{3}$	5.553		−0.380	1.52	2.53	
penta-BeS_2	$P\bar{4}2_1m$	4.666		−0.554	2.61	3.79	

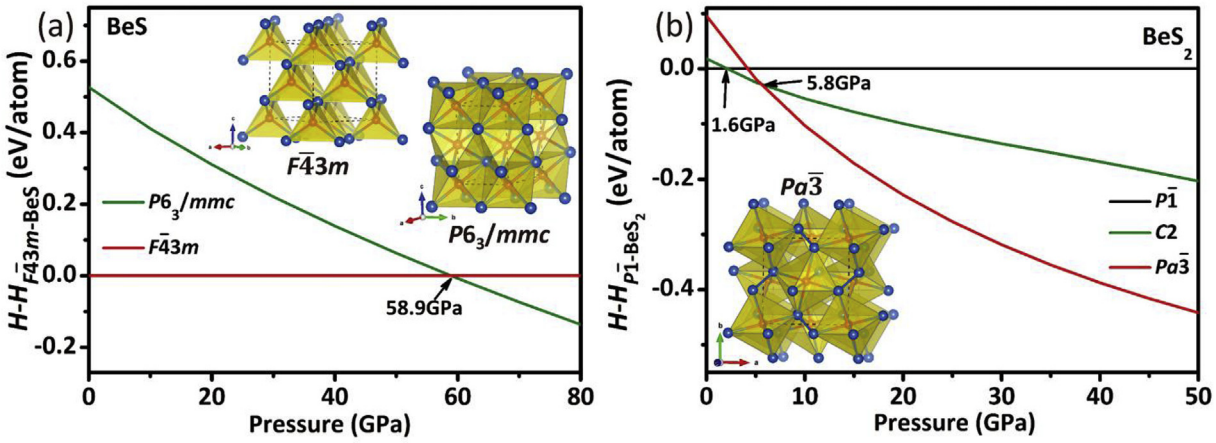

Fig. 2. Formation enthalpies difference (a) relative to $F\bar{4}3m$ phase for BeS and (b) relative to $P\bar{1}$ phase for BeS_2 as a function of pressure. The crystal structures of $F\bar{4}3m$-, $P6_3/mmc$-BeS (*c*-,*h*-BeS) and $Pa\bar{3}$-BeS_2 (*c*-BeS_2) polyhedron view are shown in (a) and (b), respectively. Red and blue spheres indicate Be and S atoms, respectively. (For interpretation of the references to colour in this figure legend, the reader is referred to the Web version of this article.)

be seen that zinc-blende-type BeS forms the perfect BeS_4 (SBe_4) tetrahedron within the unique Be-S bond length, 2.114 Å. Four adjacent BeS_4 tetrahedrons are linked together by sharing one S atom, then stacked in columns paralleling to *c* direction. The high pressure phase, *h*-BeS, can be characterized as BeS_6 octahedrons stacked along [001] direction by face-sharing. Each Be atom sits in the center of the octahedron with the equal Be-S bond length (2.321 Å). Thus, the increasing of the coordination numbers from four to six was observed for BeS phases under pressure. The bigger Be-S separation in the *h*-BeS could be aroused from the increasing coordination numbers as well.

Intriguingly, a hitherto unreported pyrite-type BeS_2 (S.G. $Pa\bar{3}$, donated as *c*-BeS_2) becomes thermodynamically stable above 25 GPa (see in Figs. 1b and 2b). BeS_2 firstly adopts $P\bar{1}$ structure (Fig. 2b), then transforms into *C*2 phase at about 1.6 GPa. Subsequently, *C*2 phase transforms into $Pa\bar{3}$ phase at about 5.8 GPa. The lattice parameters and crystal structures of $P\bar{1}$ and *C*2 BeS_2 are shown in Table S1 and Fig. S1. It is possible to obtain $P\bar{1}$- and *C*2-BeS_2 in the electrochemical process, owing to their preference to the low pressure. *c*-BeS_2 appears on the convex hull at about 25 GPa, and it is energetically preferred at least up to 100 GPa. The pyrite-type BeS_2 is stable at pressures well within the current reach of high-pressure apparatuses. It can be expected that, similar to other pyrite-type compounds(i.e. FeS_2 [46] and PtN_2 [47]), *c*-BeS_2 once obtained may be recovered to ambient conditions. From Fig. 3a, *c*-BeS_2 has a simple cubic structure with one equivalent Be occupying the position at 4a (0.000, 0.500, 0.500) and one equivalent S at 8c (0.392, 0.108, 0.892) site. This structure is similar to NaCl structure, where Be takes the position of the cation sites and S_2 takes the position of the anion sites. The most striking feature of this structure is that each S atom is tetrahedrally coordinated by three Be atoms and meanwhile bonded with another S atom, forming exotic quasi-molecular S_2 units, just like the S_2 dimers in pyrite-FeS_2 [46], the O_2 units existing in pyrite-BeO_2 [48] and N_2 dimers in PtN_2 [47], acting as persulfide ion (S_2^{2-}). The bond length of S_2 dimer is 2.071 Å, which is comparable to 2.065 Å and 2.086 Å in NiS_2 and MnS_2 [49], respectively, slightly shorter than that in FeS_2 (2.16 Å) [50]. The S-S bond length in S_2 dimers is also larger than that in SI (2.06 Å) [40], which may come from the existence of the S-S antibonding states (see later). From polyhedron point of view (Fig. 2b), as same as *h*-BeS, each Be atom in *c*-BeS_2 is sixfold coordinated by S atoms, forming the ideal octahedron with equal Be-S bond (2.337 Å) at 0 GPa, very close to that in *h*-BeS (2.321 Å), longer than that in *c*-BeS (2.114 Å). The octahedrons (BeS_6) are interconnected with sulfur atoms by vertex sharing and S_2 dimers. We note that pyrite-FeS_2 has been demonstrated to be potential electrode material with theoretical specific capacity of 894 $mAhg^{-1}$ [51], therefore, the electrochemical property of isostructural BeS_2 deserves further research.

Due to the large volume changing of electrodes during charge and discharge process, the nano-scaled materials with layer structures usually exhibit better cycling performance in comparison with the counterpart bulk materials [52]. Therefore, two dimensional layered structures for BeS and BeS_2 were also explored here. As shown in Fig. 1a, there are bilayer and monolayer structures obtained from our structural researches: $P\bar{3}m1$-BeS (donated as T-BeS) and $P\bar{4}2_1m$-BeS_2 (donated as penta-BeS_2) stand out from the massive structure searching, respectively. Note that both layer phases are not sitting on the line of convex hull, while it is not surprising as 2D materials are usually metastable structures. For example, borophene is metastable by 0.56 eV/atom with respect to bulk phase, but it was synthesized experimentally on single crystal Ag [53,54]. What's more, ΔH_f of T-BeS phase is −0.922 eV/atom, higher than the $F\bar{4}3m$ bulk phase by only 0.103 eV/atom, and lower than that of the 2D H-BeS by 0.084 eV/atom, which was proposed previously by Jin et al. [45] ΔH_f of penta-BeS_2 is −0.554 eV/atom, about 0.122 eV/atom above the convex-hull, and lower than that of $Pa\bar{3}$ bulk phase, indicating the great possibility of experimental synthesis for the two layer phases.

As seen in Fig. 3c–f, T-BeS adopts a bilayer structure where the single layer is similar to *h*-BN, both Be and S atoms are fourthfold coordinated. It could been seen from Fig. 3e that the layer fluctuates with 0.614 Å, and the total thickness is 2.805 Å, on the other hand, Be atoms are sited on top of the S atoms and vice versa. The intralayer distance of Be-S bonds is 2.098 Å, which is slightly larger than 1.98 Å in H-BeS [45], shorter than the Be-S bond length in the three bulk structures discussed above, and the Be-S interlayer distance is 2.191 Å. Penta-BeS_2 is a quasi-2D structure similar with $P\bar{4}2_1m$-SiP_2 predicted by Huang et al. [55] and penta-GeP_2 predicted by Fazel et al. [56] Each Be is coordinated with four S atoms, and each S atom connects with two Be atoms and one S atom, forming a Be_2S_3 pentagon network. Fazel et al. also proposed that ΔH_f of O-GeP_2 (with orthogonal SiP_2 structure [57]) is higher than penta-GeP_2 by 0.008eV/atom. For comparison, we also build up O-BeS_2 with orthogonal SiP_2 structure (see in Fig. S1c and Table S1), however, ΔH_f of O-BeS_2 is −0.444 eV/atom, higher than penta-BeS_2

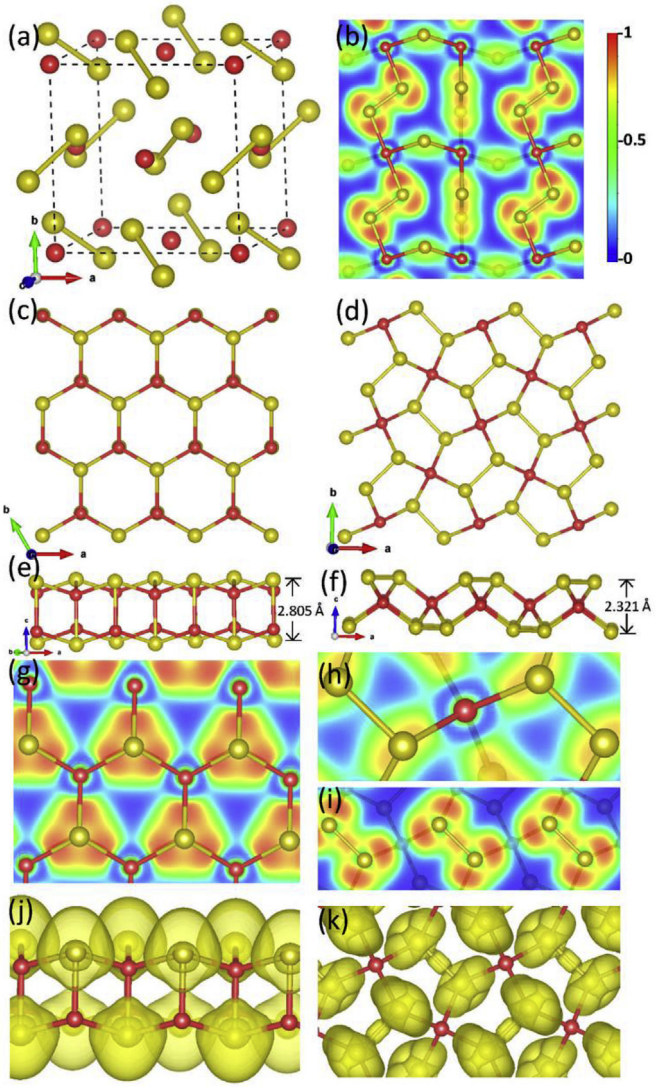

Fig. 3. Structures of (a) *c*-BeS_2, (c) and (e) T-BeS from top and side views, (d) and (f) penta-BeS_2 from top and side views. Electron localization function (ELF) for (b) *c*-BeS_2 on the plane of (−1 0 1), (g) T-BeS on the plane of (0 0 1), (h) and (i) penta-BeS_2 on the plane of (0 0 1). Side and top views of the ELF with isosurface of 0.75 for (j) T-BeS and (k) penta-BeS_2, respectively. Red and yellow spheres indicate Be and S atoms, respectively. (For interpretation of the references to colour in this figure legend, the reader is referred to the Web version of this article.)

by about 0.11 eV/atom. Therefore, O-BeS_2 is excluded here. It could be seen from Fig. 3f that the layer of penta-BeS_2 fluctuates with 1.161 Å, and the total thickness is 2.321 Å, which is slightly thinner than penta-GeP_2 (2.86 Å). From the side view, it could be seen as the well-known triple-layer structure with the Be atomic plane sandwiched by two S atomic planes, common to most of 2D transition-mental dichalcogenides, such as MoS_2 [58]. It is noteworthy that Be and S atoms are fourthfold and threefold bonded respectively, both are forming eight-electron shell closure, which could enhance the stability further. Moreover, the S-S bond length is 2.106 Å (slightly longer than the 2.071 Å S-S bond length in *c*-BeS_2), and the Be-S bond length is 2.103 Å (comparable to that in T-BeS), so the Be_2S_3 penta-rings are close to equilateral pentagons.

Furthermore, as shown in Fig. 4, the phonon spectra were calculated to determine the dynamic stability for the sulfides. There is no imaginary frequency observed in the entire Brillouin zone for the identified phases, indicating their dynamical stability in the considered pressure range.

To get more insight into the bonding features of these phases, the Electron Localization Function (ELF) are depicted in Fig. 3 and Fig. S2. As expected, S atoms show the pronounced electron localizations, agreeing well with the higher electronegativity of S (2.58) atom than Be atom (1.57), indicating the strong ionic character for Be-S bonds. Bader charge analysis also confirms that about 1.6*e* were transferred from Be atom to S atom, for all considered beryllium sulfides here, which is closed to the ideal 2*e* for S^{2-} or S_2^{2-}, supporting the S^{2-}/S_2^{2-} anions nature in BeS/BeS_2. However, this electron transfer also indicates the slightly covalent bonding for Be-S bonding, which has been provided by previous results as well [18,59]. On the other hand, for S-S bonding (in *c*-BeS_2 and penta-BeS_2), the significant electron can be seen between two S atoms in Fig. 3b, i and k. The ELF value of greater than 0.75 between S dimers indicates a strong nonpolar covalent bonding.

The calculated band structures at ambient condition are shown in Fig. 5, Figs. S3 and S4. It can be seen that *c*-BeS is a semiconductor with indirect band gap of 3.14 eV (Fig. S3a), in good agreement with previous theoretical results [42,43], and lower than the experimental result [18], due to the underestimations of PBE calculations (see in Table 1). *h*-BeS is also an indirect semiconductor with band gap of 1.45 eV at 0 GPa in our calculation (Fig. S3b), which is very close to the optimum band gap for single-junction photovoltaic applications (1.4 eV) [60]. The band structure of predicted *c*-BeS_2 indicates the semiconducting character with a direct band gap of 1.52 eV at Γ point, larger than the indirect band gap of pyrite-FeS_2 (0.95 eV) [61]. It could be observed that the four single bands along the Γ-M line always degenerate to one band along the M-R line, similar with the CN_2 in pyrite structure [62]. The orbital analyses reveal that the valence band maximum (VBM) at Γ point is mainly

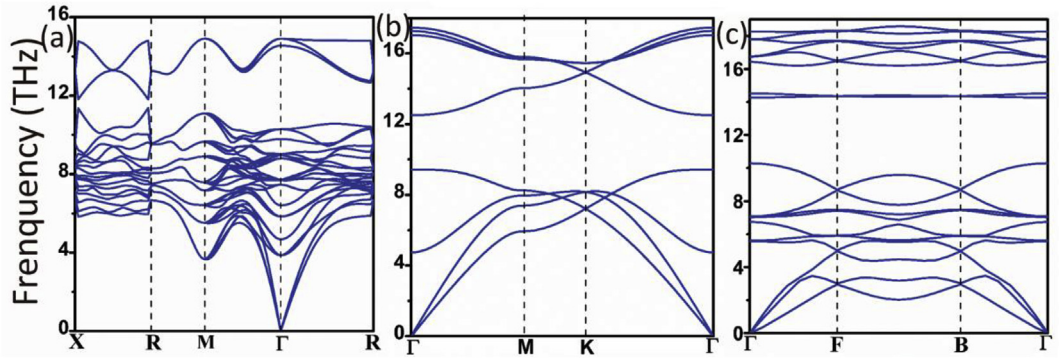

Fig. 4. Phonon dispersion curves of *c*-BeS_2 (a), T-BeS (b) and penta-BeS_2 (c).

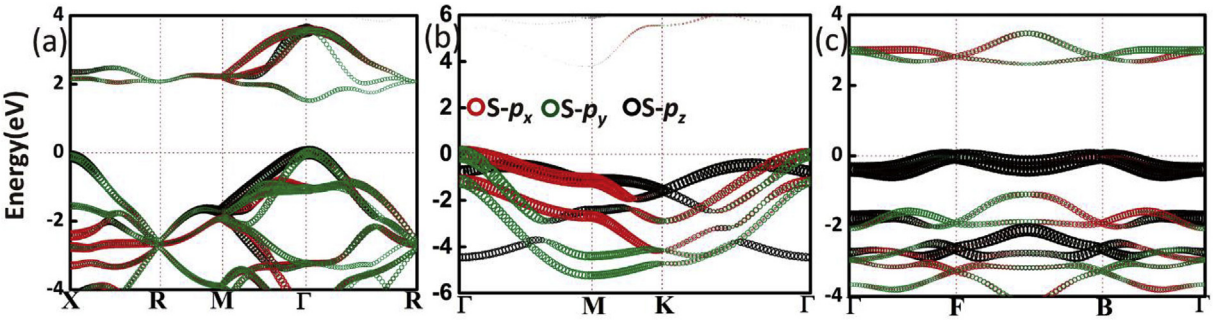

Fig. 5. The band structures for *c*-BeS_2 (a), T-BeS (b) and penta-BeS_2 (c).

composed of S-p_y and p_z orbitals, while the conduction band minimum (CBM) at Γ point is dominated by S-p_x, p_y and p_z orbitals. For the bilayer T-BeS, it is an indirect semiconductor with band gap of 3.79 eV, smaller than the indirect band gap of H-BeS (4.26 eV) mentioned above [45]. The VBM at Γ point is mainly composed of S-p_x and p_y orbitals, while S atoms have almost no contributions for the CBM at M point. For the monolayer penta-BeS_2, it is also an indirect semiconductor with band gap of 2.61 eV, larger than that of MoS_2 (1.9eV) [63]. The VBM at F and B points are mainly contributed by S-p_z orbitals while the main contributions of CBM between F and B points are from S-p_y orbitals.

In order to provide further insights into the stability and physical properties, the density of states (DOS) and COHP curves are plotted in Fig. 6 and Fig. S5. Notably, for these five phases, there is a common feature that S-*p* orbitals (p_z orbitals, in particular) are almost dominated near the Fermi level (E_F). For *c*-BeS, the S-p_x orbitals are dominant in the energy interval of −5.8 to −3.9 eV, wherein the hybridizations between Be-*s* states and S-*p* states (including p_x and p_y) make contribution to the structural stability. While the states in the energy range from −3.9 to −2.6 eV are dominated by S-p_y orbital, then S-p_z orbital is dominant from −2.6 eV to E_F. For *h*-BeS, there are also some hybridization between Be-*s* and S-p_x, p_y in the energy range of −7.2 to −6.6 eV. The weaker hybridizations over a narrower energy range in comparison with *c* phase are in accordance with the relative smaller Be-S COHP values, which may be ascribed to the longer Be-S bond length (2.321 Å) than that of *c*-BeS (2.113 Å). For T-BeS, analogous to *c*- and *h*-BeS, Be-*s* and S-p_x, p_y states hybridize in the energy interval of −4.5 to −2.4 eV. However, there is an obvious COHP peak for the intralayer Be-S bonds at −4.2eV, indicating stronger bonding interaction of intralayer than that of the interlayer. It is also confirmed that Mulliken overlap populations (*MOP*) value is higher by 0.32 for the intralayer bonds (0.56 and 0.24 for intra- and interlayer bonds, respectively). While the bond length of interlayer bonds (2.191 Å) is just 0.093 Å shorter than that of intralayer (2.098 Å), thus the uniqueness of structure determines the stronger bonds of intralayer than interlayer. In addition, *MOP* value of Be-S bond is 0.58 for *c*-BeS, 0.32 for *h*-BeS, 0.40 for *c*-BeS_2 and 0.53 for penta-BeS_2. The relative higher Be-S *MOP* values and bonding states of Be-S bonds in COHP analysis also confirm the existence of some covalent property in Be-S bonding.

For the predicted *c*- and penta-BeS_2, significant sp^3 hybridization of S-*s*, p_x, p_y and p_z orbitals can be observed in a wide energy region of valence band (−7.2 eV to E_F for $Pa\bar{3}$- BeS_2 and -5.3 eV to E_F for $P\bar{4}2_1m$-BeS_2), originating from the robust covalent bonding of S-S dimers, as shown in the ELF analysis. In the case of COHP, it is saliency to note that the S-S bonding interaction is much stronger than that of Be-S bonding. As shown in Fig. 6a and c, the S-S bonding states is starting from −7.3 to −2.5 eV for *c*-BeS_2 and from −5.6 to −2.0 eV for penta-BeS_2, the wider bonding energy range for *c*-BeS_2 unveils the stronger S-S dimers bonding in particular pyrite structure, in line with the shorter S-S bond length of *c*-BeS_2. Simultaneously, a certain of antibonding states could be seen from −2.5 eV to E_F and from −2.0 eV to E_F for *c*- and penta-BeS_2 respectively, which are basically built up by the π^* states of S_2 dimmers occupied by the electrons transferred from Be atoms. On the other hand, the S-S *MOP* values are 0.39 and 0.38 for *c*- and penta-BeS_2, respectively. The relatively weak interactions may be originated from the antibonding states in S-S bonding.

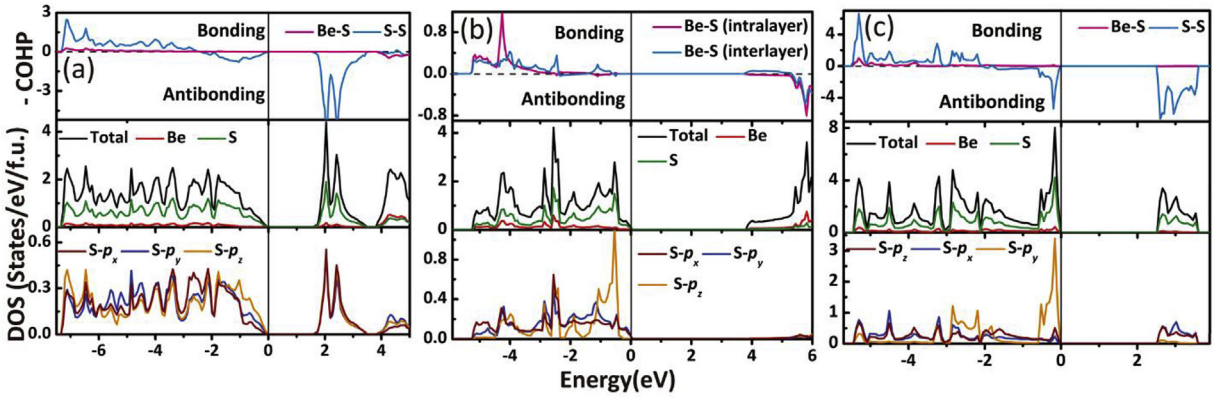

Fig. 6. The density of states (DOS) and COHP (in eV per pair) curves for *c*-BeS_2 (a), T-BeS (b) and penta-BeS_2 (c). The vertical line at zero is the Fermi energy level in DOS photographs.

4. Conclusions

In summary, we performed systematically structural predictions in the Be-S system at ambient and high pressure. A bulk structure (c-BeS_2) was identified to be stable thermodynamically and dynamically at 25 GPa. Bilayer T-BeS and monolayer penta-BeS_2 also stood out from our predictions. Furthermore, we investigated the electronic properties of the five phases on ab initio level. The results of band structures reveal that c-BeS_2 is a direct band gap semiconductor, while the others show semiconducting features with indirect band gaps. By analyzing bonding properties, it is observed that Be-S bonds hold ionic property mainly with some covalent feature, and S atoms of the two BeS_2 phases are in the form of S_2 units with strong covalent bond character. The outstanding properties make contribution to the stability and extremely large possibility to synthesis for the three phases we predicted. We have offered new possibilities of direct band gap bulk-semiconductor and indirect band gap layer-semiconductor in Be-S system, which could have potential applications in optical and electrical technologies.

Acknowledgment

This work was supported by National Natural Science Foundation of China (NSFC) under Grants No. U1530402, Thousand Youth Talents Plan, and China Postdoctoral Science Foundation (2016M601280). The numerical calculations in this paper have been done on the supercomputing system in the High Performance Computing Center of Yanshan University.

Appendix A. Supplementary data

Supplementary data to this article can be found online at https://doi.org/10.1016/j.jallcom.2018.11.374.

References

[1] X. Liang, C. Hart, Q. Pang, A. Garsuch, T. Weiss, L.F. Nazar, A highly efficient polysulfide mediator for lithium-sulfur batteries, Nat. Commun. 6 (2015) 5682.
[2] L.F. Nazar, M. Cuisinier, Q. Pang, Lithium-sulfur batteries, MRS Bull. 39 (2014) 436–442.
[3] Q. Pang, X. Liang, C.Y. Kwok, L.F. Nazar, Advances in lithium-sulfur batteries based on multifunctional cathodes and electrolytes, Nat. Energy 1 (2016) 16132.
[4] Y.X. Wang, J. Yang, S.L. Chou, H.K. Liu, W. Zhang, D. Zhao, S.X. Dou, Uniform yolk-shell iron sulfide-carbon nanospheres for superior sodium-iron sulfide batteries, Nat. Commun. 6 (2015) 8689.
[5] X. Yu, A. Manthiram, Ambient-temperature sodium-sulfur batteries with a sodiated nafion membrane and a carbon nanofiber-activated carbon composite electrode, Adv. Energy Mater. 5 (2015), 1500350.
[6] W. Li, S. Cheng, J. Wang, Y. Qiu, Z. Zheng, H. Lin, S. Nanda, Q. Ma, Y. Xu, F. Ye, Synthesis, crystal structure, and electrochemical properties of a simple magnesium electrolyte for magnesium/sulfur batteries, Angew Chem. Int. Ed. Engl. 128 (2016) 6406–6410.
[7] Z. Zhao-Karger, X. Zhao, D. Wang, T. Diemant, R.J. Behm, M. Fichtner, Performance improvement of magnesium sulfur batteries with modified non-nucleophilic electrolytes, Adv. Energy Mater. 5 (2015), 1401155.
[8] Z. Zhang, Z. Cui, L. Qiao, J. Guan, H. Xu, X. Wang, P. Hu, H. Du, S. Li, X. Zhou, Novel design concepts of efficient Mg-ion electrolytes toward high-performance magnesium-selenium and magnesium-sulfur batteries, Adv. Energy Mater. 7 (2017), 1602055.
[9] A. Manthiram, Y. Fu, S.H. Chung, C. Zu, Y.S. Su, Rechargeable lithium-sulfur batteries, Chem. Rev. 114 (2015) 11751–11787.
[10] P.G. Bruce, S.A. Freunberger, L.J. Hardwick, J.M. Tarascon, Li-O_2 and Li-S batteries with high energy storage, Nat. Mater. 11 (2011) 19–29.
[11] S. Xin, Y.X. Yin, Y.G. Guo, L.J. Wan, A high-energy room-temperature sodium-sulfur battery, Adv. Mater. 26 (2014) 1261–1265.
[12] X. Yu, A. Manthiram, Performance enhancement and mechanistic studies of magnesium-sulfur (Mg-S) cells with an advanced cathode structure, ACS Energy Lett. 1 (2016) 431–437.
[13] A.D. Hwang, A.M. Mebel, Theoretical study of the reversible storage of H_2 by BeS, chem, Phys. Lett. 122 (2000) 11406–11410.
[14] M. Chen, Q. Zhang, M. Zhou, D.M. Andrada, G. Frenking, Carbon monoxide bonding with BeO and $BeCO_3$: surprisingly high CO stretching frequency of $OCBeCO_3$, Angew. Chem. 127 (2015) 126–130.
[15] M. Arrowsmith, H. Braunschweig, M.A. Celik, T. Dellermann, R.D. Dewhurst, W.C. Ewing, H. Kai, T. Kramer, I. Krummenacher, J. Mies, Neutral zero-valent s-block complexes with strong multiple bonding, Nat. Chem. 8 (2016) 638.
[16] W.M. Yim, J.P. Dismukes, E.J. Stofko, R.J. Paff, Synthesis and dome properties of BeTe, BeSe and BeS, Solid State Commun. 9 (1972) 501–505.
[17] H. Luo, K. Ghandehari, R.G. Greene, A.L. Ruoff, S.S. Trail, F.J. Disalvo, Phase transformation of BeSe and BeTe to the NiAs structure at high pressure, Phys. Rev. B 52 (1995) 7058–7064.
[18] C. Narayana, V.J. Nesamony, A.L. Ruoff, Phase transformation of BeS and equation-of-state studies to 96 GPa, Phys. Rev. B 56 (1997) 14338–14343.
[19] L.B. Tepper, H.L. Hardy, R.I. Chamberlin, Toxicity of beryllium compounds, Br. J. Ind. Med. 19 (1962) 147.
[20] A.B. Dermer, M.L. Green, K.J. Mascaritolo, M.C. Heaven, Photoelectron velocity map imaging spectroscopy of the beryllium sulfide anion, BeS^-, J. Phys. Chem. A 121 (2017) 5645–5650.
[21] J. Jalilian, M. Safari, Electronic and optical properties of beryllium sulfide monolayer: under stress and strain conditions, Phys. Lett. A 380 (2016) 3546–3552.
[22] Y. An, T. Wang, Z. Fu, X. Chu, G. Xu, The electronic transport properties of graphene-like beryllium sulfide nanoribbons, Phys. Lett. A 379 (2015) 1837–1841.
[23] N. Benosman, N. Amrane, S. Méçabih, H. Aourag, Structural and electronic properties of bulk BeS, J. Phys. Chem. Solids 65 (2004) 1871–1878.
[24] A. Waag, F. Fischer, K. Schull, T. Baron, H.J. Lugauer, T. Litz, U. Zehnder, W. Ossau, T. Gerhard, M. Keim, Laser diodes based on beryllium-chalcogenides, Appl. Phys. Lett. 70 (1997) 280–282.
[25] Y. Wang, J. Lv, Z. Li, Y. Ma, CALYPSO: a method for crystal structure prediction, Comput. Phys. Commun. 183 (2012) 2063–2070.
[26] Y. Wang, J. Lv, L. Zhu, Y. Ma, Crystal structure prediction via Particle swarm optimization, Phys. Rev. B 82 (2010) 7174–7182.
[27] G. Kresse, J. Furthmüller, Efficient iterative schemes for ab initio total-energy calculations using a plane-wave basis set, Phys. Rev. B 54 (1996) 11169.
[28] J.P. Perdew, K. Burke, M. Ernzerhof, Generalized gradient approximation made simple, Phys. Rev. Lett. 78 (1997) 3865.
[29] J.E. Peralta, J. Heyd, G.E. Scuseria, R.L. Martin, Spin-orbit splittings and energy band gaps calculated with the Heyd-Scuseria-Ernzerhof screened hybrid functional, Phys. Rev. B 74 (2006), 073101.
[30] J. Heyd, G.E. Scuseria, M. Ernzerhof, Erratum: "Hybrid functionals based on a screened Coulomb potential", J. Chem. Phys. 124 (2006), 219906.
[31] P.E. Blöchl, Projector augmented-wave method, Phys. Rev. B 50 (1994) 17953–17979.
[32] D.J. Chadi, Special points for Brillouin-zone integrations, Phys. Rev. B 16 (1977) 5188–5192.
[33] A. Togo, I. Tanaka, First principles phonon calculations in materials science, Scripta Mater. 108 (2015) 1–5.
[34] R. Dronskowski, P.E. Bloechl, Crystal orbital Hamilton populations (COHP): energy-resolved visualization of chemical bonding in solids based on density-functional calculations, J. Phys. Chem. 97 (1993) 8617–8624.
[35] A.D. Becke, K.E. Edgecombe, A simple measure of electron localization in atomic and molecular systems, J. Chem. Phys. 92 (1990) 5397–5403.
[36] G. Henkelman, A. Arnaldsson, H. Jónsson, A fast and robust algorithm for Bader decomposition of charge density, Comput. Mater. Sci. 36 (2006) 354–360.
[37] M.D. Segall, R. Shah, C.J. Pickard, M.C. Payne, Population analysis of plane-wave electronic structure calculations of bulk materials, Phys. Rev. B 54 (1996) 16317.
[38] M.D. Segall, P.J.D. Lindan, M.J.A. Probert, C.J. Pickard, P.J. Hasnip, S.J. Clark, M.C. Payne, First-principles simulation: ideas, illustrations and the CASTEP code, J. Phys. Condens. Matter 14 (2002) 2717.
[39] K. Momma, F. Izumi, VESTA: a three-dimensional visualization system for electronic and structural analysis, J. Appl. Crystallogr. 41 (2008) 653–658.
[40] H. Fujihisa, Y. Akahama, H. Kawamura, H. Yamawaki, M. Sakashita, T. Yamada, K. Honda, T.L. Bihan, Spiral chain structure of high pressure selenium-II and sulfur-II from powder x-ray diffraction, Phys. Rev. B 70 (2004), 134106.
[41] D. Rached, M. Rabah, N. Benkhettou, R. Khenata, B. Soudini, Y. Al-Douri, H. Baltache, First-principle study of structural, electronic and elastic properties of beryllium chalcogenides BeS, BeSe and BeTe, Comput. Mater. Sci. 37 (2006) 292–299.
[42] D. Heciri, L. Beldi, S. Drablia, H. Meradji, N.E. Derradji, H. Belkhir, B. Bouhafs, First-principles elastic constants and electronic structure of beryllium chalcogenides BeS, BeSe and BeTe, Comput. Mater. Sci. 38 (2007) 609–617.
[43] C.M.I. Okoye, Structural, electronic, and optical properties of beryllium monochalcogenides, Eur. Phys. J. B 39 (2004) 5–17.
[44] M. González-Díaz, P. Rodríguez-Hernández, A. Muñoz, Elastic constants and electronic structure of beryllium chalcogenides BeS, BeSe, and BeTe from first-principles calculations, Phys. Rev. B 55 (1997) 14043–14046.
[45] J. Yu, W. Guo, Two-dimensional hexagonal beryllium sulfide crystal, J. Phys. Chem. Lett. 4 (2013) 1856–1860.
[46] J. Hu, Y. Zhang, M. Law, R. Wu, First-principles studies of the electronic properties of native and substitutional anionic defects in bulk iron pyrite, Phys. Rev. B 85 (2012), 085203.
[47] R. Yu, Q. Zhan, X.F. Zhang, Elastic stability and electronic structure of pyrite

type PtN_2: ahard semiconductor, Appl. Phys. Lett. 88 (2006) 294–913.
[48] S. Zhang, L. Fei, H. Xu, G. Yang, Pressure-induced stable beryllium peroxide, Inorg. Chem. 56 (2017) 5233–5238.
[49] N. Elliott, Interatomic distances in FeS_2, CoS_2, and NiS_2, J. Chem. Phys. 33 (1960) 903–905.
[50] E.D. Stevens, M.L. Delucia, P. Coppens, Experimental observation of the effect of crystal field splitting on the electron density distribution of iron pyrite, Cheminform 11 (1980) 813–820.
[51] E. Strauss, G. Ardel, V. Livshits, L. Burstein, D. Golodnitsky, E. Peled, Lithium polymer electrolyte pyrite rechargeable battery: comparative characterization of natural pyrite from different sources as cathode material, J. Power Sources 88 (2000) 206–218.
[52] X. Xu, W. Liu, Y. Kim, J. Cho, Nanostructured transition metal sulfides for lithium ion batteries: progress and challenges, Nano Today 9 (2014) 604–630.
[53] A. Lherbier, A.R. Botelloméndez, J.C. Charlier, Electronic and optical properties of pristine and oxidized borophene, 2D Mater. 3 (2016), 045006.
[54] B. Peng, H. Zhang, H. Shao, Y. Xu, R. Zhang, H. Zhu, Electronic, optical, and thermodynamic properties of borophene from first-principle calculations, J. Mater. Chem. C 4 (2016) 3592–3598.
[55] B. Huang, H.L. Zhuang, M. Yoon, B.G. Sumpter, S.H. Wei, Highly stable two-dimensional silicon phosphides: different stoichiometries and exotic electronic properties, Phys. Rev. B 91 (2015), 121401.
[56] F. Shojaei, J.R. Hahn, H.S. Kang, Electronic structure and photocatalytic band offset of few-layer GeP_2, J. Mater. Chem. A 5 (2017) 22146–22155.
[57] T. Wadsten, M. Vikan, C. Krohn, N. Åke, H. Theorell, R. Blinc, S. Paušak, L. Ehrenberg, J. Dumanović, The crystal structures of SiP_2, $SiAs_2$, and GeP, Acta Chem. Scand. 21 (1967) 593–594.
[58] G.Q. Huang, Z.W. Xing, D.Y. Xing, Dynamical stability and superconductivity of Li-intercalated bilayer MoS_2: a first-principles prediction, Phys. Rev. B 93 (2016), 104511.
[59] F. Wang, M. Zhou, P. Zhou, Z. Zheng, Ab-initio study of phase stability, thermodynamic and elastic properties of beryllium sulfide under extreme condition, J. Alloys Compd. 554 (2013) 363–370.
[60] S. William, J.Q. Hans, Detailed balance limit of efficiency of p-n junction solar cells, J. Appl. Phys. 32 (1961) 510–519.
[61] A. Ennaoui, S. Fiechter, C. Pettenkofer, N. Alonso-Vante, K. Büker, M. Bronold, C. Höpfner, H. Tributsch, Iron disulfide for solar energy conversion, Sol. Energy Mater. Sol. C 29 (1993) 289–370.
[62] R. Weihrich, V. Eyert, S.F. Matar, Structure and electronic properties of new model dinitride systems: a density-functional study of CN_2, SiN_2, and GeN_2, Chem. Phys. Lett. 373 (2003) 636–641.
[63] H.J. Conley, B. Wang, J.I. Ziegler, R.F.J. Haglund, S.T. Pantelides, K.I. Bolotin, Bandgap engineering of strained monolayer and bilayer MoS_2, Nano Lett. 13 (2013) 3626.